Ocean Engineering 165 (2018) 438–449

Contents lists available at ScienceDirect

Ocean Engineering

journal homepage: www.elsevier.com/locate/oceaneng

Improvement of maneuverability in a VLCC by a high lift rudder

Mochammad Zaky*, Masaaki Sano, Hironori Yasukawa

Hiroshima University, Higashi-Hiroshima, Japan

ARTICLE INFO

Keywords:
Ship maneuverability
High lift rudder
Maneuvering simulations
MMG model

ABSTRACT

In this study, the improvement of maneuverability of a Very Large Crude oil Carrier (VLCC) with small engine output under a condition involving 30% reduced EEDI [IMO (2012)] was performed by attaching a high lift rudder. A high lift rudder (HL rudder) with a fishtail section and end plates was newly designed to increase the rudder force under a restriction that minimizes the increase in rudder resistance. Tank tests were performed by using a scaled ship model with a HL rudder to capture propulsive performance and rudder force characteristics of the ship with a HL rudder. The results indicated that the designed HL rudder increased the effective rudder force by approximately 10% when compared to a conventional mariner rudder (MN rudder). The incorporation of the test results into the MMG simulation model [Yasukawa and Yoshimura (2015a)] allowed the performance of maneuvering simulations in calm water and adverse weather conditions for a ship with HL and MN rudders. The results indicated that the HL rudder presented in this study is useful in improving maneuverability while maintaining almost the same level as the propulsive performance of a ship with a mariner rudder.

1. Introduction

The International Maritime Organization (IMO) requires that all ships above 400 GT must reduce Energy Efficiency Design Index (EEDI) by a maximum of 30% after 2025 IMO (2011). The employment of a small main engine output is an extremely effective way to lower fuel consumption and to reduce CO_2 emissions. However, small engine output may lead to a low propeller load, and thereby reduces the rudder force. Therefore, an excessive reduction in the engine output results in a potentially unexpected unsafe situation in which a helms man is unable to adequately maneuver a ship in adverse weather conditions.

Yasukawa et al. (2017) studied the effect of small main engine output on maneuverability of a Very Large Crude oil Carrier (VLCC) in still water and adverse weather conditions. In the study, the initial design of a VLCC involved 30% EEDI reduced (Step3) as opposed to a conventional VLCC (Step0) by employing energy saving devices, a large diameter propeller, and a low output engine with an electronic control. The results confirmed that the maneuverability of Step3 was worse than that in Step0 with respect to time-domain maneuvering simulations. In the simulations, problems that did not comply with IMO maneuvering criteria IMO (2002a), IMO (2002b) did not occur although the engine output was reduced in Step3. This was because a conventional ship (Step0) initially possessed good maneuverability, and a sufficient margin existed for the IMO criteria. Accordingly, a reduction in the main engine output (due to advances in energy-saving technology) based on a situation in which a ship faces limitation in terms of the IMO criteria could lead to a possibility in which maneuverability worsens until an unacceptable level is reached in terms of navigational safety through a reduction in the rudder force. In this case, measures are required to ensure that maneuverability does not worsen through given further advances in energy savings.

As one of the counter-measure, a rudder with special sectional shape (special rudder) is applied for achieving the high lift rudder force in this paper. The high lift rudder improves the ship maneuverability certainly. Several studies examined the impact of a special rudder on maneuvering and propulsive performances of ships. Bingham and Mackey (1987) reviewed the maneuvering performance of ships with a high lift rudder, such as the Schilling rudder and a flap rudder, and indicated that the Schilling rudder exhibited better turning ability, was simpler in construction, and cheaper when compared with the flap rudder. Brix (1993) indicated that the rudder with various fishtails section produces a larger lift force as compared to the NACA mariner rudder, although the drag increases at all rudder angles. The lift force of this rudder evidently improved about 8–12% when attached on a series of container ship. Hasegawa et al. (2006) investigated the course-keeping ability of a Pure Car Carrier in windy conditions for two rudders (Schilling rudder and mariner rudder), and concluded that the Schilling rudder produces a larger lift force when compared with the mariner rudder. Nagarajan et al. (2008) confirmed that maneuverability and fuel efficiency of a VLCC with a Schilling rudder were superior when

* Corresponding author.
E-mail addresses: d156358@hiroshima-u.ac.jp, marinebki1979@gmail.com (M. Zaky).

https://doi.org/10.1016/j.oceaneng.2018.07.030
Received 6 June 2017; Received in revised form 17 April 2018; Accepted 11 July 2018
Available online 02 August 2018

Nomenclature

Abbreviation

EEDI	Energy Efficiency Design Index
HL rudder	High Lift rudder
IMO	International Maritime Organization
MCR	Maximum Continuous Rating
MN rudder	Mariner rudder
NOR	Normal output
VLCC	Very Large Crude oil Carrier

Greek symbols

β	hull drift angle at midship, $\beta = \tan^{-1}(-v_m/u)$ (rad)
χ	wave direction (rad)
χ_0	relative wave direction with respect to ship heading, $\chi_0 = \chi - \psi$ (rad)
δ	rudder angle (rad)
γ_R	flow straightening coefficient (−)
η_H	hull efficiency (−)
η_R	relative rotative efficiency (−)
Λ	aspect ratio of rudder (−)
∇	displacement volume of ship (m^3)
ψ	ship heading (rad)
ρ	water density (kg m^{-3})
θ_W	wind direction (rad)

Roman symbols

A_d	advance (m)
A_e	expanded area of the propeller (m^2)
A_R	rudder area including horn (m^2)
A_X	front wind pressure area (m^2)
A_Y	side wind pressure area (m^2)
A_0	disc area of the propeller, $A_0 = \pi D_p^2/4$ (m^2)
a_H	rudder force increase factor (−)
B	ship breadth (m)
B_R	averaged rudder chord length (m)
C_b	block coefficient (−)
D	ship depth (m)
D_p	propeller diameter (m)
D_t	tactical diameter (m)
d	ship draft (m)
F_N	rudder normal force (N)
F_{nwl}	Froude number based on L_{wl} (−)
H_R	rudder span (m)
$H_{1/3}$	significant wave height (m)
I_{zG}	moment of inertia of ship around the center of gravity (kg m^2)
J_z	added moment of inertia (kg m^2)
L	ship length between perpendiculars (m)
L_{wl}	ship length waterline (m)
ℓ_R	effective longitudinal coordinate of rudder position in formula of the effective inflow angle to rudder in maneuvering motions (m)
m	ship's mass (kg)
m_x, m_y	added masses of x-axis direction and y-axis direction, respectively (kg)
N_A	yaw moment around the midship due to the wind (N m)
N_E	engine revolution at MCR (rpm)
N_H	yaw moment around the midship acting on ship hull with the exception of the added mass component (N m)
N_m	yaw moment around the midship with the exception of the added mass component (N m)
N_R	yaw moment around the midship by steering (N m)
N_W	yaw moment in irregular waves (N m)
n_P	propeller revolution (rps)
$o - xyz$	fixed coordinate system of the ship by considering the origin at the midship
$o_0 - x_0y_0z_0$	space fixed coordinate system
P_E	engine power at MCR (kW)
p	propeller pitch ratio (−)
r	yaw rate (rad s^{-1})
$\dot{r}$	yaw acceleration (rad s^{-2})
S	wetted surface area of a ship without a rudder and horn (m^2)
T_r	transfer (m)
T_v	averaged wave period (s)
t	time (s)
t_P	thrust deduction factor (−)
U	resultant speed, $U = \sqrt{u^2 + v_m^2}$ (m s^{-1})
U_0	approach speed (given speed) (m s^{-1})
u	surge velocity (m s^{-1})
u_R	longitudinal inflow velocity component to the rudder (m s^{-1})
$\dot{u}$	surge acceleration (m s^{-2})
V_s	ship speed (m s^{-2})
v_m	lateral velocity at midship (m s^{-1})
$\dot{v}_m$	lateral acceleration at the midship (m s^{-2})
w	wake fraction in the model (−)
w_s	wake fraction in full-scale (−)
X	surge force with the exception of the added mass component (N)
X_A	surge force due to the wind (N)
x_G	longitudinal position of the center of gravity of a ship (m)
X_H	surge force acting on a ship hull with the exception of the added mass component (N)
X_P	propeller force (N)
X_R	surge force by steering (N)
X_W	surge force in irregular waves (N)
x_H	longitudinal coordinate of the acting point of the additional lateral force (m)
x_R	longitudinal coordinate of the rudder position (m)
Y	lateral force with the exception of the added mass component (N)
Y_A	lateral force due to wind (N)
Y_H	lateral force acting on the ship hull with the exception of the added mass component (N)
Y_R	lateral force by steering (N)
Y_W	lateral force in irregular waves (N)
Z	number of propeller blades (−)

compared with a ship with a conventional mariner rudder. Nguyen and Ikeda (2013) numerically confirmed that a rudder with a fishtail section exhibited a higher lift when compared with a NACA mariner rudder. Liu et al. (2016) investigated the impact of the rudder section on maneuvering performance, and the results indicated that the wedge-tail section produces a larger rudder force and smaller turning indexes albeit with least efficiency (i.e., higher rudder resistance). In summary, extant studies indicated that a rudder with a fishtail or a wedge-tail section similar to a Shilling rudder can potentially be used as a measure to improve maneuverability, although there is a possibility that the propulsive performance is worsened due to increase of the rudder resistance. To minimize the rudder resistance increase, in this paper, a

high lift rudder with small rudder area is newly designed.

This study involved performing an improvement in the maneuverability of a VLCC with small engine output under a condition with 30% reduced EEDI IMO (2012) by attaching a high lift rudder as an extension of a previous study Yasukawa et al. (2017). Extant studies did not investigate the effect of a high lift rudder on the maneuverability of a ship in adverse weather conditions with respect to small engine output. First, a high lift rudder with a fishtail section and end plates was designed to increase the rudder force under a restriction that minimized the rudder resistance increase. The new rudder is termed as a HL rudder in this study. Conversely, the original mariner rudder is termed as a MN rudder. This is followed by performing tank tests by using a scaled ship model (model length: 2.909 m) to capture the propulsive performance and rudder force characteristics of a ship with MN and HL rudders. The incorporation of the test results into the MMG simulation model Yasukawa and Yoshimura (2015a) led to the performance of maneuvering simulations in calm water and adverse weather conditions for a VLCC with a HL rudder ($Step3_{HL}$) and MN rudder ($Step3_{MN}$). For the purposes of comparison, maneuvering simulations were also performed for Step0 with a MN rudder. It should be noted that the prediction accuracy of the simulation method was confirmed by performing a comparison with free-running test results Yasukawa and Yoshimura (2015a) and Yasukawa et al. (2015b). For reference, comparisons of turning trajectories between experiment and calculation in calm water and irregular waves are shown in Figs. 1 and 2. The agreement between experiment and calculation is acceptable in view of practical purposes. The study discussed the effect of a high lift rudder on maneuverability based on simulation results from a navigation safety viewpoint.

2. Ship used in the study

In this study, the target ship corresponded to a VLCC titled KVLCC2 SIMMAN (2008) in which hull form data was previously published Yasukawa et al. (2017). Table 1 lists the principal particulars of the ship. In the table, L denotes length between perpendiculars, L_{wl} denotes length of the waterline, B denotes breadth, D denotes depth, d denotes draft, ∇ denotes displacement volume, S denotes wetted surface area without a rudder and a horn, x_G denotes longitudinal position of the center of gravity (fore position from the midship is positive), and C_b denotes the block coefficient. The load condition involved a full load even keel. Fig. 3 illustrates the body plan.

Fig. 4 shows side and front views including the super-structure of the ship used in the study. The configuration and arrangement of the super-structure were estimated based on an existing VLCC tanker with a similar size since an actual full-scale ship corresponding to KVLCC2 was not available. The front wind pressure area A_X corresponds to 1,161 m^2, and the side wind pressure area corresponds to A_Y 4,258 m^2.

Table 2 shows a summary of EEDI, the main engine output, the revolution, and propeller specifics for Step0 and Step3 Yasukawa et al. (2017). In the study, Step0 is with respect to a conventional VLCC that corresponds to the base ship and Step3 corresponds to a VLCC with 30% reduced EEDI. In the table, P_E denotes engine power at Maximum Continuous Rating (MCR), N_E denotes engine revolution at MCR, D_P denotes propeller diameter, p denotes propeller pitch ratio, A_e/A_0 denotes expanded area ratio, and Z denotes the number of blades. The propeller was designed such that it achieved a ship speed of 15.5 knots in the normal output (NOR) with a 15% sea margin based on the existing propeller diagram.

3. Design of a high lift rudder

A rudder design necessitates the consideration of certain aspects such as working conditions, parameters (area, thickness, span, and aspect ratio), sectional shape, structural arrangement, and hydrodynamic interactions (among hull, propeller, and rudder). Significantly, the selection of the parameters and sectional shape impact ship maneuverability Bertram (2012). Existing studies Liu et al. (2016), Nguyen and Ikeda (2013), Nagarajan et al. (2008) indicate that a special rudder with a fishtail section produced a larger rudder force and smaller turning indexes when compared to those of a mariner rudder. A rounded leading edge and a fishtail trailing edge were employed as the sectional shape of the present HL rudder. Additionally, slipstream guide plates fitted to top and bottom of the rudder were used. The plates will increase the lift gradient, and it was experimentally investigated by Tachi and Endo (1996). Fig. 5 shows the profiles of MN and HL rudders in a full-scale. Table 3 shows the principal particulars of MN and HL rudders. In the table, H_R denotes span of the rudder, B_R denotes averaged chord of the rudder, Λ denotes the aspect ratio, A_R denotes rudder area including the horn, and $A_R/(Ld)$ denotes rudder area ratio. The rudder area of the HL rudder is approximately 30% less than that of MN rudder. Its aim involves reducing the rudder resistance of the HL rudder. With a reduction in the rudder area of HL rudder, it is expected to minimize the rudder torque, although the rudder torque in HL rudder may be increased due to fishtail section and end plates effect. Additionally, thinner thickness with a taper was employed in the HL rudder to reduce the rudder resistance since a thinner profile generally exhibits a better propulsive performance when compared to a thicker profile.

Fig. 6 shows photographs of two rudders for the ship model used in the tank tests. The MN rudder incorporates a rudder horn that provides housing for a pintle to support the rudder, and otherwise the HL rudder does not possess a horn.

4. Tank tests

In order to capture the propulsive performance and rudder force characteristics of the ship with MN and HL rudders, tank tests were performed in the Hiroshima University Towing Tank (length: 100 m, width: 8 m, depth: 3.5 m) by using a scaled ship model (model length: 2.901 m, scale ratio 1/110).

4.1. Propulsive performance

Self-propulsion tests were conducted for a ship model with MN and HL rudders after completing propeller open test using a stock propeller model with 90 mm in the diameter and resistance tests by using the same ship model without a rudder. Therefore, the effect of rudder difference was captured by the difference in the self-propulsion factors such as thrust deduction factors (t_P), wake fraction (w), and relative rotative efficiency (η_R). Subsequently, the hull efficiency (η_H) was predicted by $(1-t_P)/(1-w_s)$ of the full-scale ship where w_s denotes the wake fraction in full-scale.

Fig. 7 shows the self-propulsion factors and the hull efficiency. The

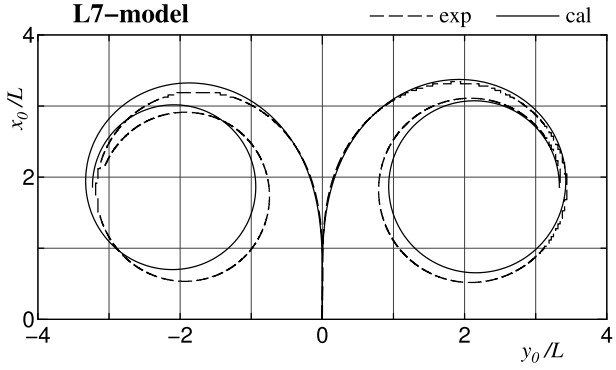

Fig. 1. Comparison of turning trajectories between experiment and calculation in calm water with $\delta = \pm 35°$ for KVLCC2 model with 7 m in model length Yasukawa and Yoshimura (2015a). The approach speed U_0 is corresponding to 15.5 knots in full-scale.

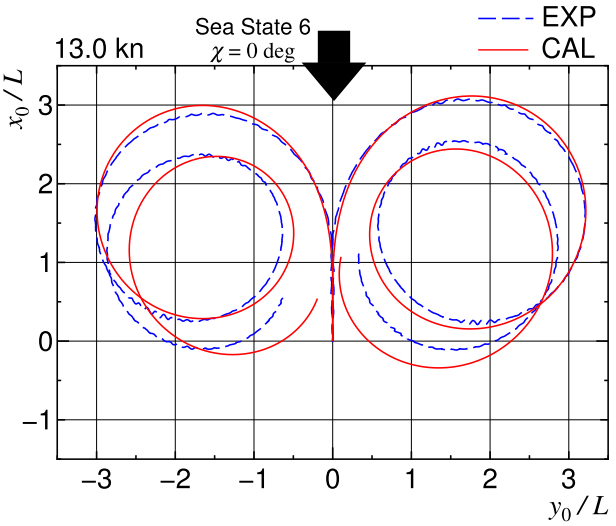

Fig. 2. Comparison of turning trajectories between experiment and calculation in short-crested irregular waves with $\delta = \pm 35°$ for KVLCC2 model with 2.90 m in model length Yasukawa et al. (2015b). The approach speed U_0 is corresponding to 13.0 knots in full-scale. Significant wave height $H_{1/3}$ is 54.5 mm, averaged wave period T_v is 0.9 s, and averaged wave direction in approaching χ is 0 deg (head waves).

Table 1
Principal particulars of the ship examined in the studied (KVLCC2).

symbol	value
L (m)	320.0
L_{wl} (m)	325.5
B (m)	58.0
D (m)	30.0
d (m)	20.80
∇ (m^3)	312,622
S (m^2)	27,178
x_G (m)	11.2
C_b	0.81

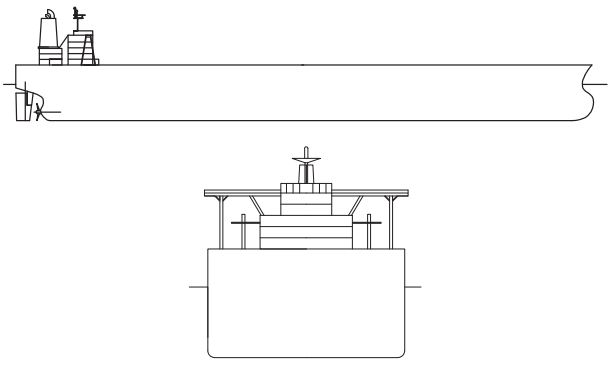

Fig. 3. Body plan of a ship used in the study (KVLCC2).

horizontal axis corresponds to the Froude number F_{nwl} based on the length waterline L_{wl}. Table 4 shows a comparison of the self-propulsion factors between MN and HL rudders at a service speed (V_s) of 15.5 knots (equivalent to $F_{nwl} = 0.141$). The ratio of wake fraction in full-scale w_s to the model w is assumed as 0.85. A high lift rudder (HL rudder) was attached, and $(1 - t_P)$ increases to approximately 5% when compared to that of the MN rudder, $(1 - w_s)$ increases by approximately 4%, η_R decreases by approximately 1%, and η_H increases by approximately 1%. The difference is small. The designed HL rudder is significantly reasonable to minimize the increase in rudder resistance.

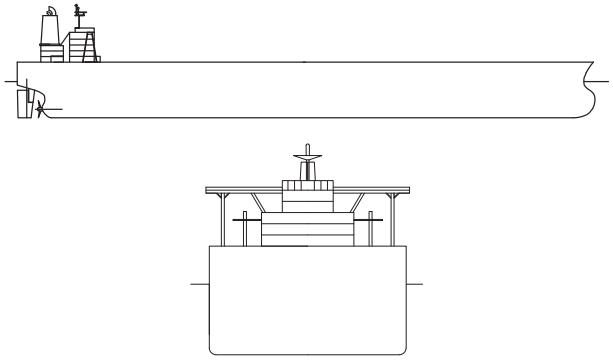

Fig. 4. Side and front views of a VLCC.

Table 2
Specifics of the Engine and propeller.

	Step0	Step3
EEDI	2.67	1.85
P_E (kW)	25,600	21,200
N_E (rpm)	76.0	61.4
D_P (m)	9.86	10.60
p	0.673	0.674
A_e/A_0	0.384	0.380
Z	4	4

4.2. Characteristics of rudder forces

Additionally, 'the rudder force test in straight moving' was performed to capture rudder force characteristics. In the test, the lateral force (Y) and yawing moment around the midship (N_m) acting on a ship hull and rudder normal force (F_N) were measured when a ship moved in a straight manner while maintaining a certain rudder angle δ. In the test, the rudder angle (δ) was changed from − 35° to 35° with an interval corresponding to 5°. The detail of the measurements is skipped here because measurement equipment, the arrangement, the procedure and the data analysis have been described in Ref. Yasukawa and Yoshimura (2015a).

Fig. 8 shows the rudder force test results for both MN and HL rudders under a propeller loading condition with $n_P = 17.2$ rps and ship model speed $U = 0.76$ m/s (equivalent to 15.5 knots in full-scale). This condition is termed as the model point. The forces (Y and F_N) and moment (N_m) are non-dimensionalized by $(1/2)\rho LdU^2$ and $(1/2)\rho L^2dU^2$, respectively, where ρ denotes water density. The absolute values of Y', N'_m, and F'_N increase linearly with increases in δ in the range of − 20° to 20°. Inclinations of Y', N'_m, and F'_N relative to the δ for the HL rudder increase when compared to those for the MN rudder. Thus, Y' and N'_m are expressed as follows:

$$\left.\begin{aligned} Y' &= Y'_\delta \delta \\ N'_m &= N'_\delta \delta \end{aligned}\right\} \quad (1)$$

where Y'_δ denotes rudder force derivative, N'_δ denotes turning moment derivative, and δ denotes rudder angle in radians. Table 5 shows the derivatives determined based on the measured data in the range of − 20° to 20°. When compared to the absolute value of the MN rudder, the absolute value of Y'_δ increases by 10% in HL rudder, and the absolute value of N'_δ increases by approximately 8%. Thus, a rudder force increase of 8–10% was confirmed with respect to the HL rudder as expected.

In contrast, F'_N at the same δ increase by approximately 30% with respect to the HL rudder, and the increase ratio is significantly different from the results of Y' and N'_m. In order to clarify the reason, the measured data was analyzed based on the MMG model Yasukawa and Yoshimura (2015a). According to the MMG model, Y' and N'_m are

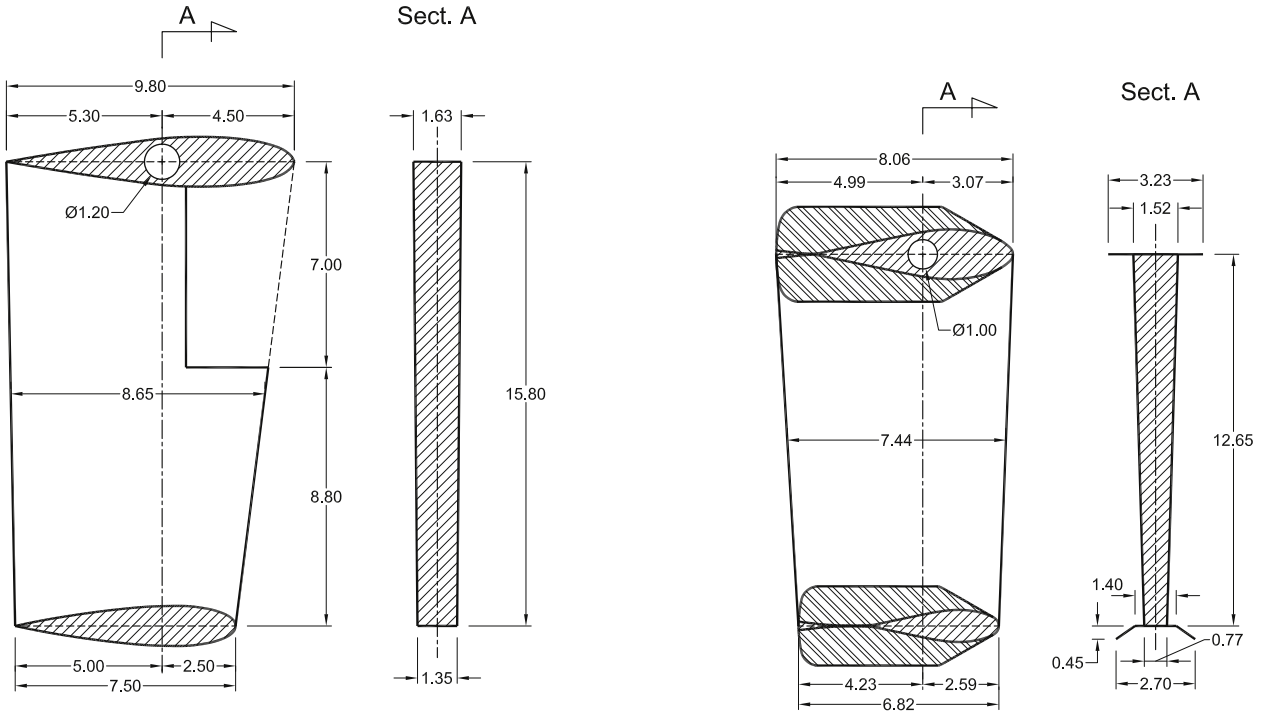

Fig. 5. Rudder profiles (left: MN rudder, right: HL rudder), units in meter.

Table 3
Principal particulars of two rudders.

	MN rudder	HL rudder	remarks
H_R (m)	15.80	12.65	
B_R (m)	8.65	7.44	including the horn part for MN rudder
Λ	1.83	1.70	including the horn part for MN rudder
A_R (m^2)	136.67	94.12	including the horn area for MN rudder
$A_R/(Ld)$	1/48.7	1/70.7	

expressed as follows:

$$\left.\begin{aligned} Y' &= -(1+a_H)F'_N\cos\delta \\ N'_m &= -(x'_R + a_H x'_H)F'_N\cos\delta \end{aligned}\right\} \quad (2)$$

where a_H denotes the rudder force increase factor, x'_R denotes the non-dimensionalized longitudinal coordinate of rudder position (normally, $x'_R \simeq -0.5$), and x'_H denotes the non-dimensionalized longitudinal coordinate of the acting point of the additional lateral force component induced by steering. $(1 + a_H)$ is determined as an inclination of Y' relative to $-F'_N\cos\delta$, and $(x'_R + a_H x'_H)$ is also determined as an inclination of N' relative to $-F'_N\cos\delta$ as shown in Fig. 9. Table 6 shows $(1 + a_H)$ and $(x'_R + a_H x'_H)$ of the MN and HL rudders. Furthermore, $(1 + a_H)$ decreases by approximately 16% in HL rudder and the absolute value of $(x'_R + a_H x'_H)$ decreases by approximately 17% when compared to those

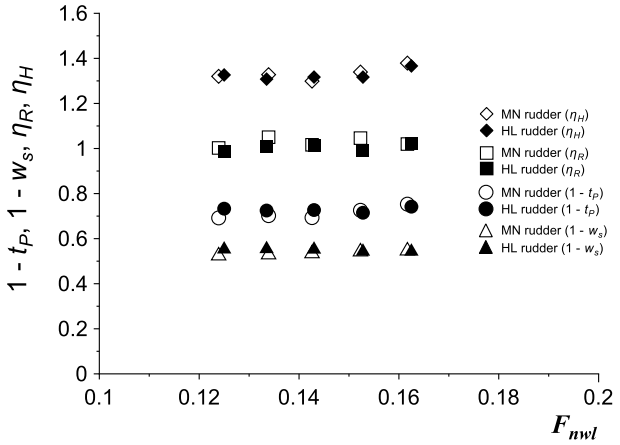

Fig. 7. Self-propulsion test results.

of the MN rudder. The effective rudder force in HL rudder is reduced by approximately 16–17% due to the hull-rudder interaction effect although the absolute value of F'_N increases by approximately 30%. Hence, the increase ratio of the effective rudder force with respect to the HL rudder actually approximately corresponds to 1.09 ($\simeq 1.30 \times (1 - 0.16)$). The order of magnitude approximately coincides

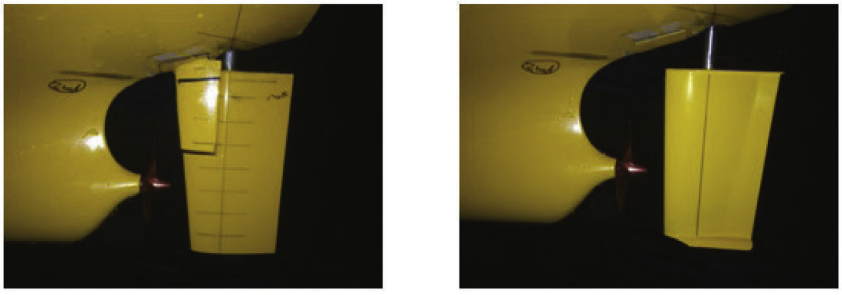

Fig. 6. Layout of the rudder (left: MN rudder, right: HL rudder).

Table 4
Self-propulsion factors and hull efficiency at V_s = 15.5 knots.

	$1-t_P$	$1-w_s$	η_R	η_H
MN rudder	0.694	0.534	1.018	1.300
HL rudder	0.727	0.552	1.014	1.316

Table 5
Rudder force and moment coefficients.

	MN rudder	HL rudder
Y'_δ	−0.0571	−0.0626
N'_δ	0.0315	0.0339

with the increase ratio of Y'_δ or N'_δ as previously mentioned. This is potentially because the HL rudder is incorporated with the horn although MN rudder is not as shown in Fig. 5. Therefore, the lift force acting on the horn part is not considered for F'_N of MN rudder. Conversely, $(1 + a_H)$ or $(x'_R + a_H x'_H)$ increases with the additional lift force.

4.3. Course stability

To observe a difference of course stability of the ship with MN and HL rudders, the course stability criterion C in calm water was compared. The criterion C is expressed as follows:

$$C = Y_v^{G'} N_r^{G'} - [Y_r^{G'} - (m' + m'_x)]N_v^{G'} \tag{3}$$

The ship becomes stable when $C > 0$ and unstable when $C < 0$. Here, $Y_v^{G'}$, $Y_r^{G'}$, $N_v^{G'}$ and $N_r^{G'}$ denote the non-dimensionalized linear hydrodynamic derivatives on maneuvering, and m' and m'_x are the non-dimensionalized mass and added mass, respectively. The derivatives correspond to the center of gravity as converted from midship point and include the effect of propeller and rudder, and are expressed as follows:

$$\left.\begin{aligned} Y_v^{G'} &= Y'_v - k_Y u'_R \gamma_R \\ Y_r^{G'} &= Y'_r - Y'_v x'_G - k_Y u'_R \gamma_R \ell'_R \\ N_v^{G'} &= N'_v - Y'_v x'_G + k_N u'_R \gamma_R \\ N_r^{G'} &= N'_r - Y'_r x'_G - (N'_v - Y'_v x'_G) x'_G + k_N u'_R \gamma_R \ell'_R \end{aligned}\right\} \tag{4}$$

$$\left.\begin{aligned} k_Y &= -Y'_\delta / u'^2_R \\ k_N &= N'_\delta / u'^2_R \end{aligned}\right\} \tag{5}$$

where u'_R is non-dimensionalized longitudinal inflow velocity component to the rudder, and assumed to be 1.0. γ_R is the flow straightening coefficient, and ℓ'_R is non-dimensional effective longitudinal coordinate of rudder position in formula of the effective inflow angle to rudder in maneuvering motions. The last term of Eq. (4) represents the rudder effect. The difference between MN and HL rudders in the linear derivatives appears as a change of k_Y and k_N. As shown in Eq. (5), k_Y and k_N

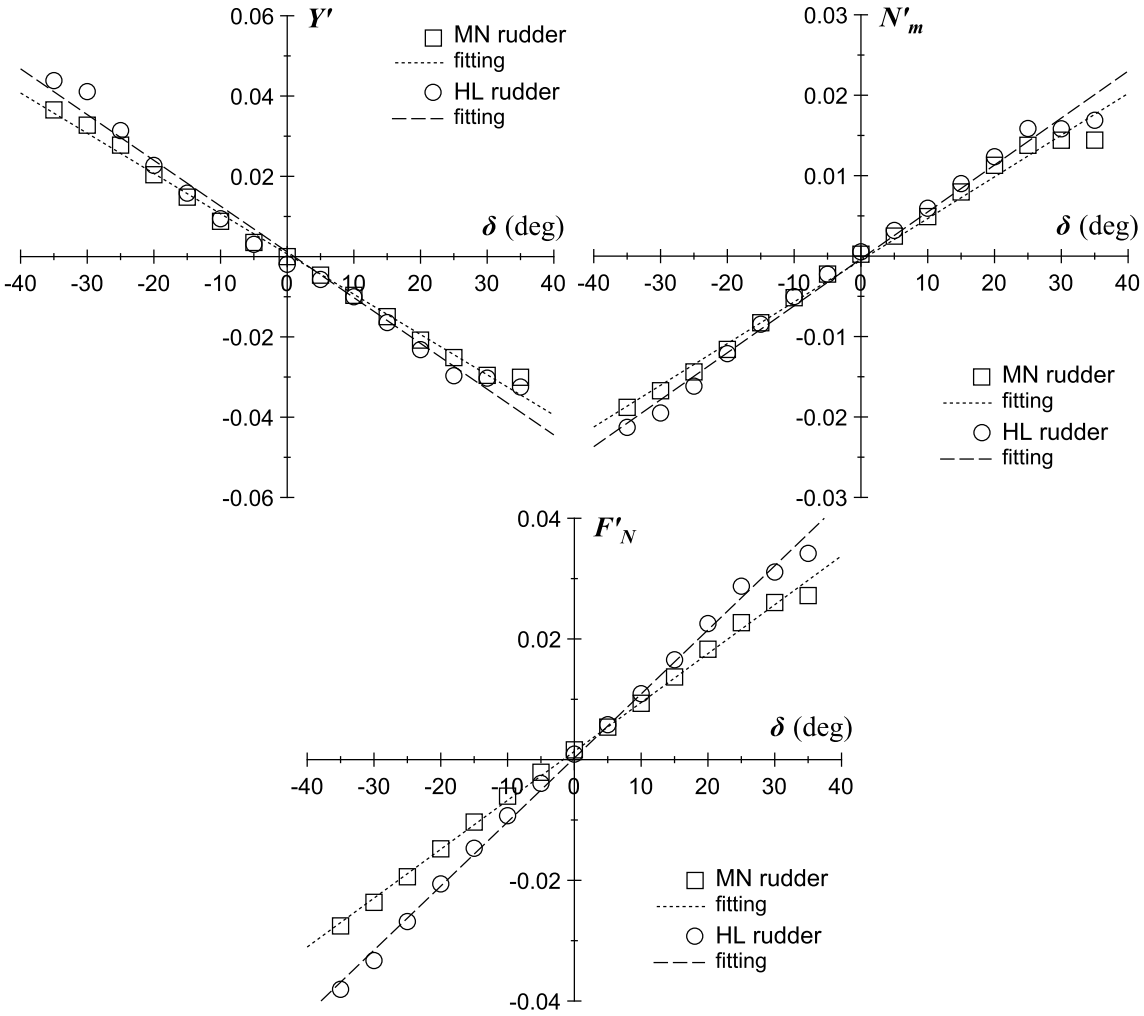

Fig. 8. Lateral force coefficient acting on a ship hull (Y'), yawing moment coefficient around the midship (N'_m) and rudder normal force coefficient (F'_N) in the rudder force test versus rudder angle δ.

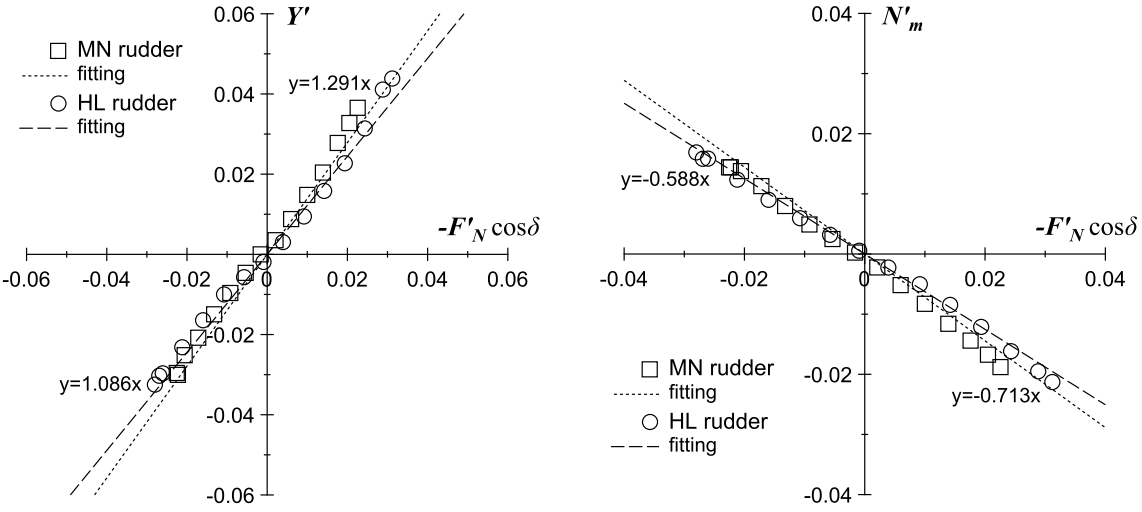

Fig. 9. Analysis results with respect to the hull and rudder interaction coefficients.

Table 6
Hull and rudder interaction coefficients.

	MN rudder	HL rudder
$1 + a_H$	1.291	1.086
$x'_R + a_H x'_H$	−0.713	−0.588

are equivalent to the rudder force and moment coefficients (Y'_δ, N'_δ). Table 7 shows the calculation results of k_Y and k_N, the linear derivatives and C for ship with MN and HL rudders. The hydrodynamic derivatives and parameters required for the calculation of C except Y'_δ and N'_δ have been shown in Ref. Yasukawa and Yoshimura (2015a). Y'_δ and N'_δ were indicated in Table 5. The C in MN rudder (Step3_{MN}) is −0.002 and HL rudder (Step3_{HL}) is −0.001. Thus, it confirmed that the ship with HL rudder is slightly more stable for course keeping. However, the difference is small.

5. Maneuvering simulations

5.1. Motion equations

Fig. 10 shows the coordinate systems used in the study. Specifically, the space-fixed coordinate system is denoted as $o_0 - x_0y_0z_0$ in which the $x_0 - y_0$ plane coincides with the still water surface, and the z_0-axis points vertically downward. The moving ship-fixed coordinate system is denoted as $o - xyz$ in which o is considered on the midship of the ship, and x, y, and z-axes point toward the ship's bow, i.e., toward the starboard and vertically downward directions, respectively. The heading angle ψ is defined as the angle between the x_0 and x-axes. Furthermore, δ denotes the rudder angle, and r denotes the yaw rate. Additionally, u and v_m denotes the velocity components in x and y directions, respectively. The drift angle at the midship position is defined as $\beta(=\tan^{-1}(-v_m/u))$. The total velocity corresponds to $U(=\sqrt{u^2 + v_m^2})$.

The main wave propagation direction is denoted as χ as shown in Fig. 10. Subsequently, relative wave direction χ_0 is defined as $\chi_0 \equiv \chi - \psi$. The head wave, the beam wave, and the following wave of the ship are defined as $\chi_0 = 0°$, $\chi_0 = 90°$, and $\chi_0 = 180°$, respectively. The wind direction θ_W is assumed as same as the wave direction χ.

The motion equations with respect to surge, sway, and yaw are expressed as follows Yasukawa and Yoshimura (2015a):

$$\left.\begin{aligned}(m + m_x)\dot{u} - (m + m_y)v_m r - x_G m r^2 &= X\\ (m + m_y)\dot{v}_m + (m + m_x)ur + x_G m\dot{r} &= Y\\ (I_{zG} + x_G^2 m + J_z)\dot{r} + x_G m\dot{v}_m + x_G mur &= N\end{aligned}\right\} \quad (6)$$

where m denotes mass of the ship, I_{zG} denotes moment of inertia around center of gravity, m_x and m_y denote added masses of x-axis direction and y-axis direction, respectively, and J_z denotes the added moment of inertia. Eq. (6) denotes the equations of motion to be solved. The unknown variables corresponded to u, v_m, and r. Additionally, X, Y, and N in the right hand side of Eq. (6) denote the surge force, lateral force, and yaw moment, respectively, around the midship with the exception of the added mass components and are expressed as follows:

$$\left.\begin{aligned}X &= X_H + X_R + X_P + X_W + X_A\\ Y &= Y_H + Y_R + Y_W + Y_A\\ N &= N_H + N_R + N_W + N_A\end{aligned}\right\} \quad (7)$$

Specifically, subscripts H, R, and P denote the hull, rudder, and propeller, respectively. The forces with subscripts H, R, and P are predicted by using the MMG model Yasukawa and Yoshimura (2015a). The subscript W denotes the wave-induced steady forces in irregular waves, and A denotes the wind forces, and this is predicted with the same conditions as those used in a previous study Yasukawa et al.(2017). Note that the hydrodynamic interaction components between hull and rudder represented by the parameters a_H and x_H as shown in Section 4.2 are included in Y_R and N_R referring to the MMG model Yasukawa and Yoshimura (2015a). The motion equation, i.e., Eq. (6), is solved, and thus it is numerically possible to determine the maneuvering motions of the ship.

5.2. Simulation outline

In the maneuvering simulations of full-scale ship with the HL rudder, the initial approach speed U_0 corresponds to 15.5 knots (navigation full condition), the rudder steering rate corresponds to 2.34°/s, and the radius of yaw gyration corresponds to 0.25 L. The engine and propeller used are the same as those in the ship with MN rudder

Table 7
Hydrodynamic coefficients and C.

	MN rudder	HL rudder
k_Y	0.057	0.063
k_N	0.032	0.034
$Y_v^{G'}$	−0.345	−0.347
$Y_r^{G'}$	0.115	0.117
$N_v^{G'}$	−0.110	−0.108
$N_r^{G'}$	−0.059	−0.060
C	−0.002	−0.001

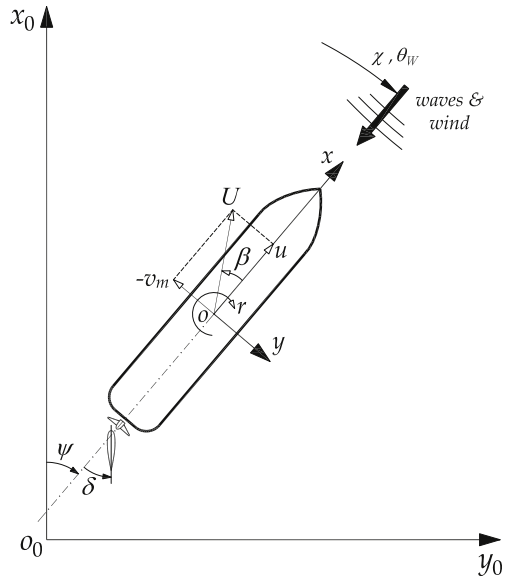

Fig. 10. Coordinate systems.

Table 8
Wind and wave conditions in the simulations.

BF	U_W (m/s)	$H_{1/3}$ (m)	T_v (s)
7	15.6	4.0	7.7
8	19.0	5.5	9.1
9	22.7	7.0	10.2

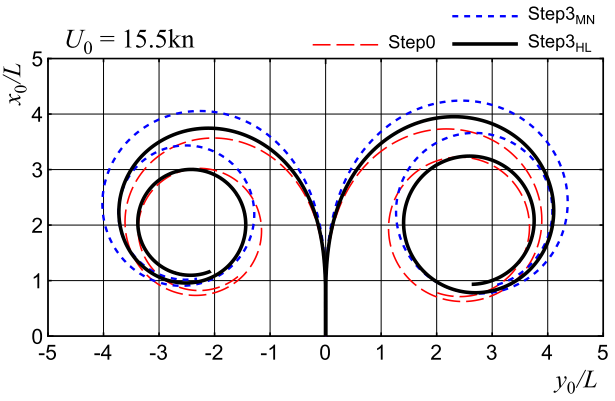

Fig. 11. A comparison of turning trajectories in calm water ($\delta = \pm 35°$).

Table 9
A comparison of turning indexes.

	$\delta = 35°$		$\delta = -35°$	
	A_d/L	D_t/L	A_d/L	D_t/L
Step3$_{MN}$	4.18	4.29	3.99	3.95
Step3$_{HL}$	3.89	4.04	3.68	3.65
Step0	3.67	3.83	3.50	3.54
IMO criteria	4.50	5.00	4.50	5.00

together with the torque limit model Yasukawa et al. (2017). Propeller revolution n_P is assumed to be constant except a case over the restrictions placed by the torque limit. The hydrodynamic treatments in the simulations are summarized as follows:

- A 30% increase in the rudder normal force (F_N) is used for the simulations based on the test result indicated in section 4.
- Given the a_H and x'_H, the measured values as shown in Table 6 are used, and
- With the exception of F_N, a_H, and x'_H, the hydrodynamic parameters used are the same as those in the ship with the MN rudder Yasukawa et al. (2017).

The environmental parameters are set based on the Beaufort scale. Table 8 shows the wind power class of the Beaufort scale (BF) used in the simulations in adverse conditions. The table shows the absolute wind speed (denoted as U_W), significant wave height (denoted as $H_{1/3}$), average wave period (denoted as T_v). The wind and waves are assumed as constant with respect to time, and the wind direction (θ_W) is same as the wave direction (χ).

5.3. Turning in calm water

Fig. 11 shows a comparison of turning trajectories between Step0, Step3$_{MN}$, and Step3$_{HL}$ given a rudder angle of ± 35°. Step0 denotes a conventional VLCC, and Step3$_{MN}$ and Step3$_{HL}$ denote a VLCC with a MN rudder and a HL rudder, respectively, under a condition with 30% reduced EEDI.

Table 9 shows a comparison of turning indexes such as advances (A_d) and tactical diameters (D_t). When compared to Step0, the turning radius in Step3$_{MN}$ increases, and A_d and D_t increase by 14% and 12%, respectively, and correspond to the averaged value of port and starboard turning. The reduction in the rudder normal force (F_N) causes the deterioration in the turning performance Yasukawa et al. (2017). This is due to the low propeller load that results from the small engine output. When compared to Step3$_{MN}$, the turning radius in Step3$_{HL}$ decreases, and A_d and D_t decrease by approximately 7% as the average values of port and starboard turning, respectively.

Thus, a significant improvement of the turning performance is confirmed by attaching the high lift rudder. The turning indexes (A_d, D_t) in Step3$_{HL}$ satisfy the IMO maneuvering criteria IMO (2002a), IMO (2002b) with a sufficient margin although they slightly exceed those in Step0. The turning performance of Step3$_{HL}$ is not at a potentially problematic level.

5.4. Zig-zag maneuvers in calm water

Fig. 12 shows the time histories of heading angle ψ and rudder angle δ in 10/10 and − 10/− 10 zig-zag maneuvers in calm water. Additionally, Fig. 13 shows the time histories of ψ and δ during 20/20 and − 20/− 20 zig-zag maneuvers.

To confirm the effect of HL rudder during zig-zag maneuvers, a comparison of rudder normal force (F_N) between MN and HL rudders is also shown in Figs. 12 and 13. Step3$_{HL}$ has the larger absolute values of F_N than Step3$_{MN}$ at the time of rudder angle changes from port side to starboard side and vice versa, and is close to the Step0 in all cases. This indicates that HL rudder produces a larger lift force than MN rudder as expected. Tables 10 and 11 depict a comparison of overshoot angle (OSA) during the zig-zag maneuvers. The OSAs of Step3$_{MN}$ exceed those of Step0, and the course stability evidently worsens. The average value of the 1st OSA in 10/10 and −10/-10 zig-zag maneuvers increases by 23% in Step3$_{MN}$, and the average value of 2nd OSA also increases by 43%. The reduction in the rudder normal force (F_N) led to an increase in the OSAs as mentioned in 5.3. Conversely, the OSA in Step3$_{HL}$ is smaller than that of Step3$_{MN}$. The average value of the 1st OSA in 10/10 and −10/-10 zig-zag maneuvers decreases by 22% in Step3$_{HL}$, and the average value of 2nd OSA also decreases by 33%. The high lift rudder is useful in significantly reducing the OSAs in zig-zag maneuvers. It should be noted that the IMO maneuvering criterion IMO (2002a), IMO (2002b) is fulfilled in all the cases.

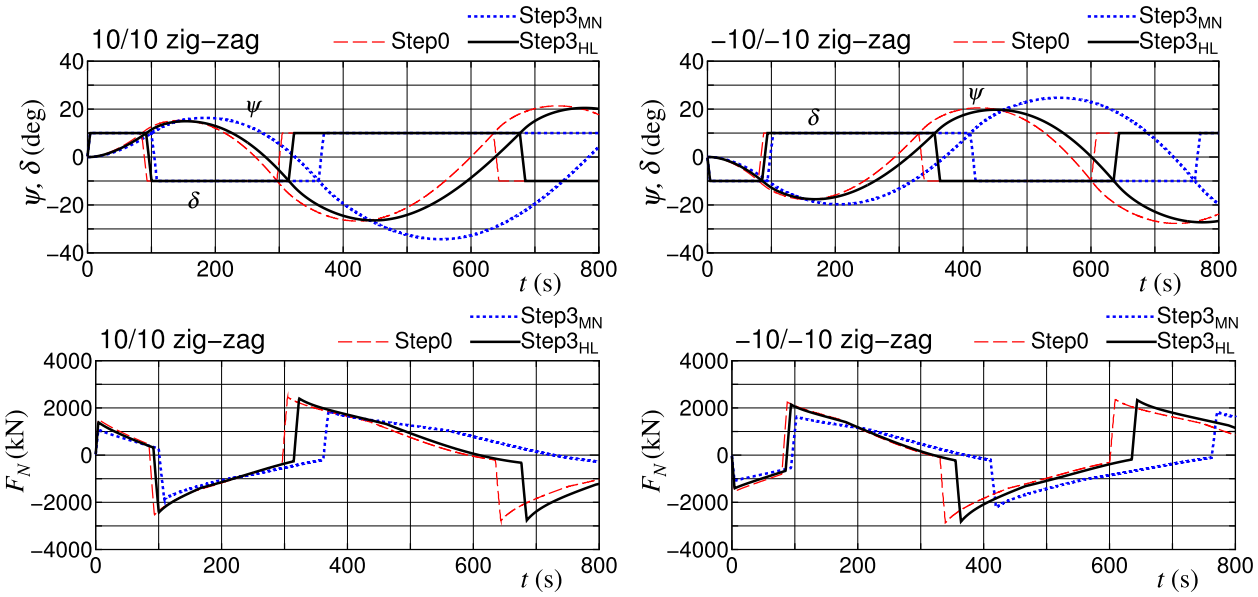

Fig. 12. A comparison of time histories of heading angle (ψ), rudder angle (δ), and rudder normal force (F_N) in calm water (left: 10/10 zig-zag, right: −10/-10 zig-zag).

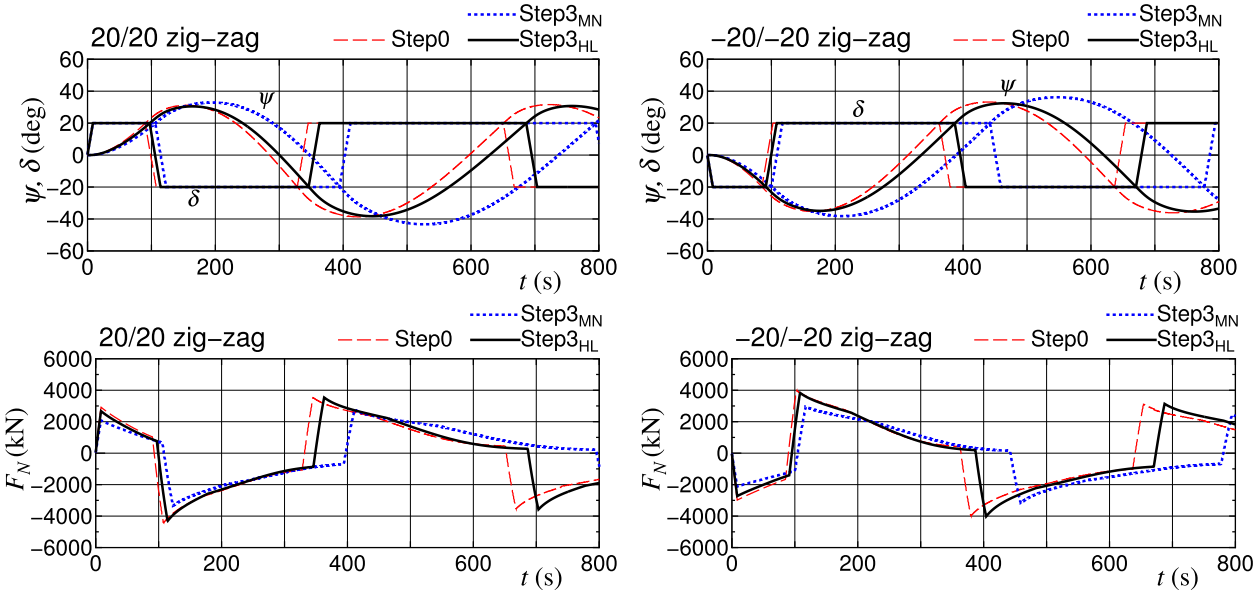

Fig. 13. A comparison of time histories of heading angle (ψ), rudder angle (δ), and rudder normal force (F_N) in calm water (left: 20/20 zig-zag, right: −20/-20 zig-zag).

Table 10
A comparison of overshoot angle of 10/10 and −10/-10 zig-zag maneuvers in calm water.

	10/10 zig-zag		−10/-10 zig-zag	
	1st OSA (°)	2nd OSA (°)	1st OSA (°)	2nd OSA (°)
$Step3_{MN}$	6.3	24.3	9.7	14.7
$Step3_{HL}$	4.9	16.4	7.6	9.7
Step0	5.3	16.7	7.8	10.5
IMO criteria	20.0	40.0	20.0	40.0

5.5. Steady state sailing conditions in adverse weather conditions

A ship traveling with a propeller revolution in the design speed is considered under wind and waves using the auto-pilot. In the auto-pilot, the PD control is applied with a proportional gain corresponding to 5.0 and a differential gain corresponding to 20.0 s. The adverse conditions in the simulation correspond to the environmental parameters (wind and waves) which were based on Beaufort scale as mentioned in Table 8.

Fig. 14 shows the longitudinal component of the ship speed (denoted as u), hull drift angle (denoted as β), and check helm (denoted as δ) in the steady state sailing condition under wind and waves for $Step3_{MN}$ and $Step3_{HL}$. In the figure, additional lines are inserted to connect the calculation results for purposes of distinction. A significant decrease in speed occurs with an increase in the BF scale. The speed decreases in $Step3_{HL}$ are almost the same as those in $Step3_{MN}$. In $\chi_0 = 0°$ of BF9, u is less than 8 knots for both, and the propeller revolution decreases due to the restrictions placed by the torque limit. The β and absolute value of δ increase with increases in the BF scale. The largest β occurs approximately at $\chi_0 = 75°$, and the smallest δ

Table 11
A comparison of overshoot angle of 20/20 and −20/-20 zig-zag maneuvers in calm water.

	20/20 zig-zag		−20/-20 zig-zag	
	1st OSA (°)	2nd OSA (°)	1st OSA (°)	2nd OSA (°)
$Step3_{MN}$	12.9	23.4	18.2	16.2
$Step3_{HL}$	10.5	18.3	14.9	12.4
Step0	11.2	18.7	15.3	13.2
IMO criteria	25.0	–	25.0	–

occurs approximately at $\chi_0 = 90°$. This tendency is the same for both $Step3_{MN}$ and $Step3_{HL}$. In BF9, the maximum β approximately corresponds to 3.2°, and is almost identical in both $Step3_{MN}$ and $Step3_{HL}$. The minimum δ approximately corresponds to − 8.1° in $Step3_{HL}$ and − 10.6° in $Step3_{MN}$. Thus, the check helm of $Step3_{HL}$ is smaller than that of $Step3_{MN}$. The HL rudder is effective in reducing the check helm in adverse weather conditions.

5.6. Course changing ability in adverse weather conditions

Course changing simulations are performed by steering the rudder angle, $\delta = 20°$, in wind and waves. Fig. 15 shows a comparison of ship trajectories in BF7 and BF9. The direction of the wind and waves changes to $\chi = 0°$, 30°, and 60°. The steady state speed shown in Fig. 14 is used as an approach speed in the simulation. A course change with a significant speed decrease is observed in BF9 since the situations involved bow wind and waves. Fig. 16 shows a comparison of the non-dimensional values of advance A_d and transfer T_r in the course change with respect to the BF scale for the three different wave (wind) directions. It should be noted that "SW" shown in the horizontal axis of the figure denotes still water. Additionally, A_d and T_r in $Step3_{HL}$ are smaller than those in $Step3_{MN}$. Thus, $Step3_{HL}$ indicates better maneuverability when compared to $Step3_{MN}$. This is because $Step3_{HL}$ indicates a better turning performance in calm water when compared to $Step3_{MN}$ as discussed in Section 5.3.

6. Concluding remarks

In this study, an improvement of maneuverability of a VLCC with small engine output under a condition with 30% reduced EEDI IMO (2012) was performed by attaching a high lift rudder. First, a high lift rudder (HL rudder) with fishtail section and end plates was newly designed to increase the rudder force under a restriction that involved minimizing the rudder resistance increase. The rudder area including horn was reduced by approximately 30% when compared to the original mariner rudder (MN rudder). The tank tests confirmed that the designed HL rudder increased the effective rudder force to approximately 10% with a few delivered power increases when compared to those of MN rudder. Subsequently, time-domain simulations based on

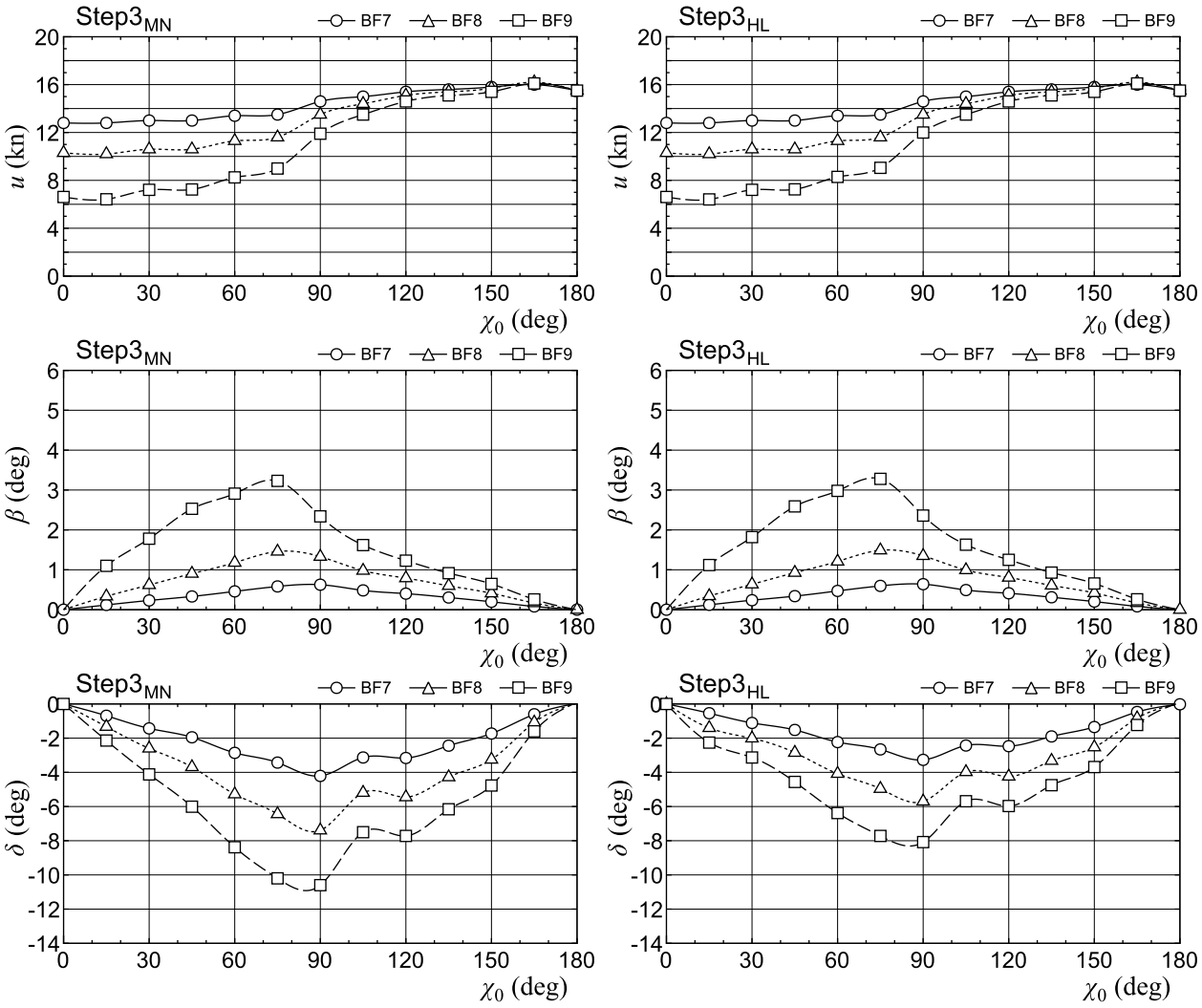

Fig. 14. A comparison of ship speed (u), drift angle (β) and check helm (δ) in wind and waves.

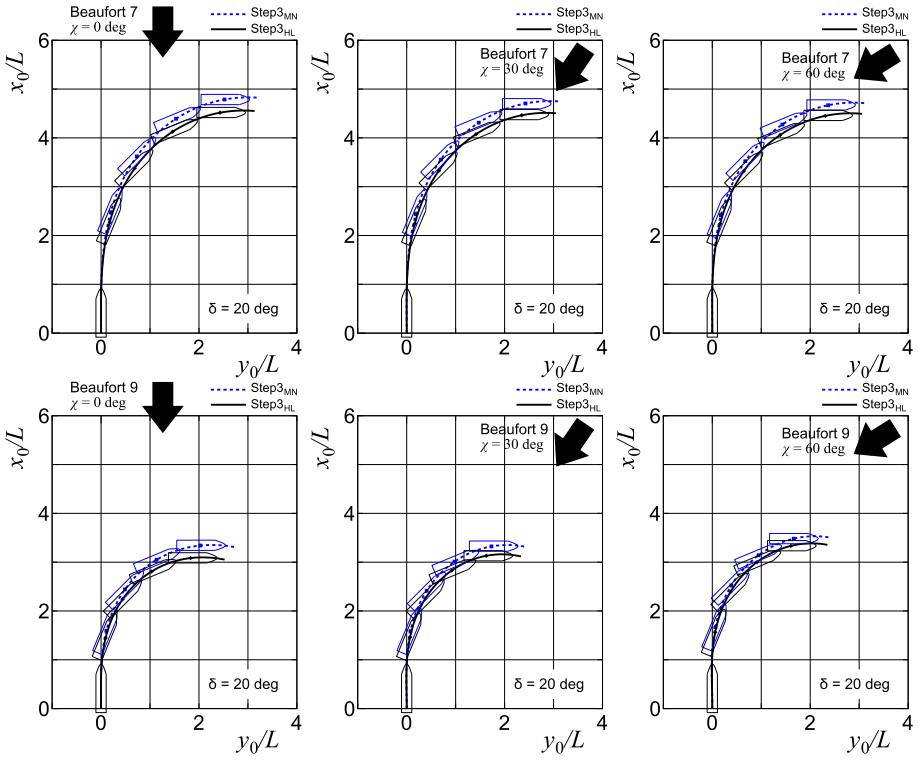

Fig. 15. Comparison of ship trajectories for course changing in wind and waves.

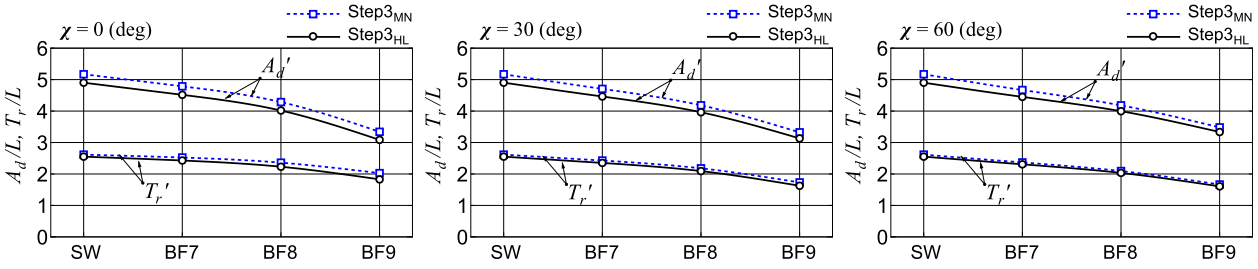

Fig. 16. Comparison of A_d and T_r in wind and waves ($\delta = 20°$).

the MMG model Yasukawa and Yoshimura (2015a) were conducted for a full-scale ship with HL and MN rudders to investigate the effect of the high lift rudder on the maneuvering motions in calm water as well as the steady state sailing condition and course changing ability in adverse weather conditions. The attachment of the HL rudder when compared to MN rudder leads to the following:

1. Advance A_d and tactical diameter D_t decreased to approximately 7% as the averaged value of port and starboard turning with a rudder angle of ± 35° in calm water.
2. The averaged 1st overshoot angle (OSA) in 10/10 and −10/-10 zig-zag maneuvers decreased by 22%, and the averaged 2nd OSA also decreased by 33%.
3. The check helm reduced by approximately 25% in adverse weather conditions, and a better course changing ability was confirmed in all the wind and wave directions.

Thus, the results indicated that a high lift rudder is useful in improving the maneuverability of the VLCC with a 30% reduction in EEDI. Further investigation is suggested to check the rudder torque of the high lift rudder.

Acknowledgement

This study was supported by JSPS KAKENHI Grant Number JP26249135, and the Fundamental Research Developing Association for Shipbuilding and Offshore (REDAS) Grant Number REDAS No.4, 2016 in Japan, and the authors appreciate individuals related to the fund. The authors express their sincere gratitude to Mr. M. Dobashi for help with the tank tests.

References

Bertram, V., 2012. Practical Ship Hydrodynamics, second ed. Elsevier Butterworth-Heinemann, Oxford.
Bingham, V.P., Mackey, T.P., 1987. High-performance rudders-with particular reference to the schilling rudder. J. Mar. Technol. 24 (4), 312–320.
Brix, J., 1993. Manoeuvring Technical Manual. Seehafen Verlag, Hamburg, Germany.
Hasegawa, K., Kang, D., Sano, M., Nagarajan, V., Yamaguchi, M., 2006. A study on Improving the Course-keeping ability of a pure car Carrier in windy conditions. J. Mar. Sci. Technol. 11 (2), 76–87.
International Maritime Organization, 2002a. Standards for ship maneuverability. Resolut. MSC 137 (76) , Accessed date: 4 December 2002.
International Maritime Organization, 2002b. Explanatory Notes to the Standards for Ship Maneuverability. MSC/Circ.1053. , Accessed date: 16 December 2002.
International Maritime Organization, 2011. Amendments to the annex of the protocol of 1997 to amend the international convention for the prevention of pollution from ships, 1973, as modified by the protocol of 1978 relating thereto, 2011. Resol. MEPC 203 (62) , Accessed date: 16 July 2011.
International Maritime Organization, 2012. 2012 guidelines on the method of calculation

on the attained energy efficiency design Index (EEDI) for new ships. Resol. MEPC 212 (63) , Accessed date: 2 March 2012.
Liu, J., Quadvlieg, F., Hekkenberg, R., 2016. Impacts of the rudder profile on maneuvering performance of ships. Ocean Eng. 124, 226–240.
Nagarajan, V., Kang, D.H., Hasegawa, K., Nabeshima, K., 2008. Comparison of the mariner schilling rudder and the mariner rudder for VLCCs in strong winds. J. Mar. Sci. Technol. 13 (1), 24–39.
Nguyen, T.V., Ikeda, Y., 2013. Hydrodynamic characteristic of rudder sections with high lift force. Conference Proceedings of JASNAOE, vol. 17. pp. 121–124 2013A-GS7-1.
SIMMAN, 2008. Part B benchmark test cases, KVLCC2 description. In: Workshop on Verification and Validation of Ship Maneuvering Simulation Method, Workshop Proceedings, vol. 1. pp. B7–B10 (2008), Copenhagen.
Tachi, K., Endo, M., 1996. Estimated manoeuvrability of T. S. Wakashio-maru-I –wind tunnel test and rudder open test– (in Japanese). J. Jpn. Inst. Navig. 94, 17–26.
Yasukawa, H., Yoshimura, Y., 2015. Introduction of MMG standard method for ship maneuvering predictions. J. Mar. Sci. Technol. 20 (1), 37–52.
Yasukawa, H., Hirata, N., Yonemasu, I., Terada, D., Matsuda, A., 2015. Maneuvering simulation of a KVLCC2 tanker in irregular waves. In: International Conference on Marine Simulation and Ship Maneuverability (MARSIM'15), Newcastle, UK, CD-R.
Yasukawa, H., Zaky, M., Yonemasu, I., Miyake, R., 2017. Effect of engine output on maneuverability of a VLCC in still water and adverse weather conditions. J. Mar. Sci. Technol. https://doi.org/10.1007/s00773-017-0435-0.